



Extending the detection and correction abilities of an adaptive optics system for free-space optical communication

Shen Zhang^a, Rui Wang^b, Yukun Wang^b, Hongmin Mao^a, Guoding Xu^a, Zhaoliang Cao^{a,*}, Xiaofei Yang^c, Wusheng Hu^d, Xiaoping Li^d, Li Xuan^b

^a Jiangsu Key Laboratory of Micro and Nano Heat Fluid Flow Technology and Energy Application, School of Physical Science and Technology, Suzhou University of Science and Technology, Suzhou, Jiangsu 215009, China

^b State Key Laboratory of Applied Optics, Changchun Institute of Optics, Fine Mechanics and Physics, Chinese Academy of Sciences, Changchun, Jilin 130033, China

^c School of Optoelectronic Science and Engineering & Collaborative Innovation Center of Suzhou Nano Science and Technology, Soochow University, Suzhou, Jiangsu 215006, China

^d Jiyuan Vocational and technical College, Jiyuan, Henan 454650, China

ARTICLE INFO

Keywords:

Adaptive optics
Strong turbulence
Free-space optical communication
Detection ability

ABSTRACT

The adaptive optics system (AOS) has been used to eliminate the effect of atmospheric turbulence for free-space optical communications. The AOSs are designed based on the statistical average performance of the turbulence. In reality, the amplitude of turbulence changes drastically, and the AOS cannot always detect and correct the aberrations appropriately. To prevent the amplitude of turbulence from exceeding the designed range of the Shack–Hartmann wavefront sensor (SH WFS), the combination of the wavefront sensorless and SH WFS methods is proposed to extend the detection range. First, the control scheme is demonstrated, and the numerical simulation is performed. Then, the validation experiments are performed with static and dynamic turbulence. Results show that the proposed method is valid and that the effective communication time is greatly lengthened.

1. Introduction

Free-space optical communication (FSOC) can change current communication methods owing to its advantages of high bandwidth and strong abilities to resist interception and interference [1–4]. However, due to the effects of the atmospheric turbulence, the communication performance of FSOC for the earth-to-satellite and horizontal links decreases greatly [5,6]. Recently, the research results show that the aerosol also affect the horizontal link performance [7]. Adaptive optics technique can overcome the distortion of atmospheric turbulence as it can correct the aberrations in a timely manner [8–10]. Many adaptive optics systems (AOSs) have been utilized for the earth-to-satellite [11–15] and horizontal links [16,17], with results indicating that the FSOC and the communication performance can be improved greatly. Furthermore, many researchers have analyzed the effects of the turbulence on the communication performance to support the AOS design of the FSOC [18–22]. Normally, the AOSs are designed based on the statistical characteristics of atmospheric turbulence, and the statistical parameters of Fried coherence length r_0 and Greenwood frequency f_G are used to design the detection spatial frequency and system control bandwidth of the AOS. Actually, the atmospheric

turbulence, especially the horizontal turbulence, is random and the aberrations can sometimes exceed the designed range of the Shack–Hartmann wavefront sensor (SH WFS) [23]. For example, in one day, the turbulence strength of daytime is much larger than that of the night. Even in a short time period, the turbulence also changes drastically. Thus, the aberrations cannot be detected and corrected appropriately, and the communication bit error rate (BER) is increased significantly. The wavefront sensorless AOSs may be selected to solve this problem as the aberrations are reconstructed by the measured images with the camera [24–26]. However, to reconstruct the wavefront accurately, all the phase retrieval algorithms require multiple iterations that take a long time to execute [27,28]. As the real time demand of the FSOC, the wavefront sensorless AOS is typically unsuitable for correcting the atmospheric turbulence. However, even though sensorless AOS has several disadvantages, it is most suitable for the task at hand.

In this paper, we propose a method to timely detect and correct the atmospheric turbulence, which is stronger than the designed value, by combining the SH WFS and the wavefront sensorless technique. First, the concrete method is demonstrated, after which a validation experiment is performed. Then, the dynamic atmospheric turbulence

* Corresponding author.

E-mail address: caozl@usts.edu.cn (Z. Cao).

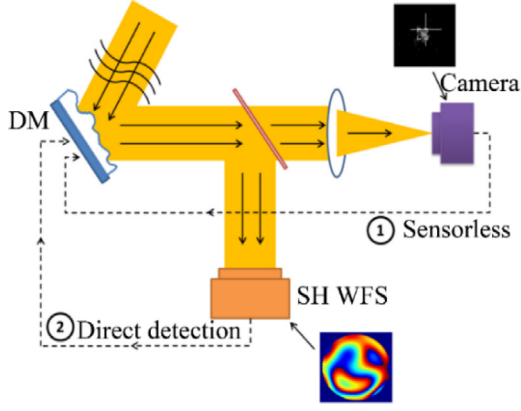


Fig. 1. Configuration for the combination of the wavefront sensorless and SH WFS modes.

produced by the turbulence simulator is corrected, and the stable laser communication is acquired. Results show the proposed method may be used to correct the turbulence, which is stronger than the designed object for the FSOC. Furthermore, compared with the ordinary AOS, the effective communication time is lengthened apparently.

2. Method

2.1. Scheme

The detection of distortion is a key procedure for the AOS. For the horizontal FSOC, the atmospheric turbulence changes drastically, and the distortions often exceed the designed detection range of SH WFS. Thus, the AOS cannot work properly as the aberrations cannot be detected correctly. To solve this problem, the combination of the SH WFS and wavefront sensorless technique is proposed, the configuration for which is shown in Fig. 1. First, the wavefront sensorless technique is used to obtain the distorted wavefront information, and the camera used to track the beacon light is utilized to acquire the image used for the wavefront reconstruction. The deformable mirror (DM) is controlled by retrieved wavefront, after which the distortions are partially corrected, and the magnitude of the aberration is reduced. While the distortions are reduced into the measurement range of SH WFS, the adaptive correction mode is immediately switched from the wavefront sensorless to the direct wavefront detection mode, and the DM is controlled by the detected wavefront with the SH WFS. As the SH WFS can measure the wavefront rapidly with high accuracy, the distortions may be corrected accurately and low communication BER is realized, while the turbulence is stronger than the designed value. Initially, the wavefront sensorless mode is used to measure and correct the large dynamic range turbulence; then, the direct detection mode is selected to realize high frequency detection and correction. Unlike the ordinary wavefront sensorless technique, we only use it at the initial stage to reduce the turbulence strength, but not to correct the turbulence at the whole communication process. Hence, the shortcomings of slow correction are acceptable. By using the wavefront sensorless technique, the turbulence may still be detected and corrected effectively even if the amplitude of the aberration exceeds the detection range of SH WFS.

The concrete control process is shown in Fig. 2, the stochastic parallel gradient descent (SPGD) algorithm is used to retrieve the aberrations according to the measured image of the camera. The aberrations are corrected by the DM, after which a switch criterion is established to determine which detection mode is chosen at the next step. Assuming the “no” instruction is sent by the switch criterion, the DM is still controlled under the wavefront sensorless mode, and the atmospheric turbulence is corrected once again. If the aberrations can be measured by the SH WFS, the switch criterion gives the “yes” instruction, and

the AOS goes into the loop that includes the SH WFS and DM. At this stage, the aberrations are detected by the SH WFS and corrected by the DM, and high frequency and accuracy correction may be realized compared with the wavefront sensorless method. With this correction scheme, the input of the algorithm is both the far field image captured by the camera and the wavefront detected with the SH WFS: first, the far field image is used to retrieve the distorted wavefront; while the SH WFS can detect the distortion rightly, the detected wavefront is selected as the input variable. As the wavefront sensorless mode is only used at the initial stage of adaptive correction, the time consumption is short and it is now possible to detect and correct stronger turbulence accurately for the FSOC.

2.2. Phase retrieval with the SPGD algorithm

For achieving wavefront sensorless AOS, the SPGD algorithm is suitable for the wavefront retrieval [29–31]. The turbulence-induced aberrations can be corrected by optimizing the system performance metric J . For a DM, the applied voltage at $(i+1)$ th iterations may be expressed as [31]

$$\bar{u}_{i+1} = \bar{u}_i + \gamma \Delta \bar{u}_i \Delta J_i, \quad (1)$$

where the voltage vector $\bar{u} = [u_1, u_2, \dots, u_N]$, in which N represents the number of actuators; γ is the descent rate, which is positive for finding a maximum of J and vice versa; ΔJ is the variation of J ; and Δu represents the applied perturbation voltages. Furthermore, Δu_i represents the uncorrelated random variables with identical amplitudes $|\Delta u_i| = a$, which obey the Bernoulli probability distribution $\Pr(\Delta u_i = \pm a) = 0.5$ [29,32].

Although the SPGD algorithm has improved the convergence speed, it is still difficult to overcome the effects of atmospheric turbulence. In this paper, the wavefront sensorless technique is just used to weaken the turbulence, but not to correct the turbulence perfectly. Consequently, to improve the convergence speed further, the Zernike polynomial method is utilized and only some low order aberrations are chosen to perform the wavefront retrieval. The wavefront may be expressed with the Zernike mode given by

$$\varphi = \sum_{j=1}^n a_j Z_j, \quad (2)$$

where a_j and Z_j are the j th coefficient and Zernike mode, respectively.

The wavefront fitted by the DM may be described by

$$\varphi_{DM} = \sum_{i=1}^k u_i R_i = [R_1, R_2, \dots, R_k] \times \begin{bmatrix} u_1 \\ u_2 \\ \vdots \\ u_k \end{bmatrix} = \bar{M} \times \bar{U}, \quad (3)$$

where R_i is the influence function of i th actuator, and \bar{M} and \bar{U} are the influence and voltage matrix, respectively. The Zernike modes are used to perform the optimization by combining Eqs. (2) and (3) as follows:

$$\varphi = \sum_{j=1}^n a_j Z_j = \bar{M} \times \bar{U}, \quad (4)$$

where the optimization object changes from the applied voltage to the Zernike coefficient. Eq. (1) may be rewritten as

$$\varphi_{i+1} = \varphi_i + \gamma \Delta \varphi_i \Delta J. \quad (5)$$

According to Eq. (5), the distortion may be corrected with the selected modes of Zernike polynomials. Moreover, the iteration speed is proportional to the mode number of Zernike polynomials. As partial correction is needed to reduce the turbulence strength, only the first few modes of the Zernike polynomial is selected to perform the optimization, thus greatly improving the convergence speed.

In the paper, the light intensity captured by the camera in a circle with the diameter of R is selected as the metric J . This can be computed as follows:

$$J = \iint_R I(x, y) dx dy. \quad (6)$$

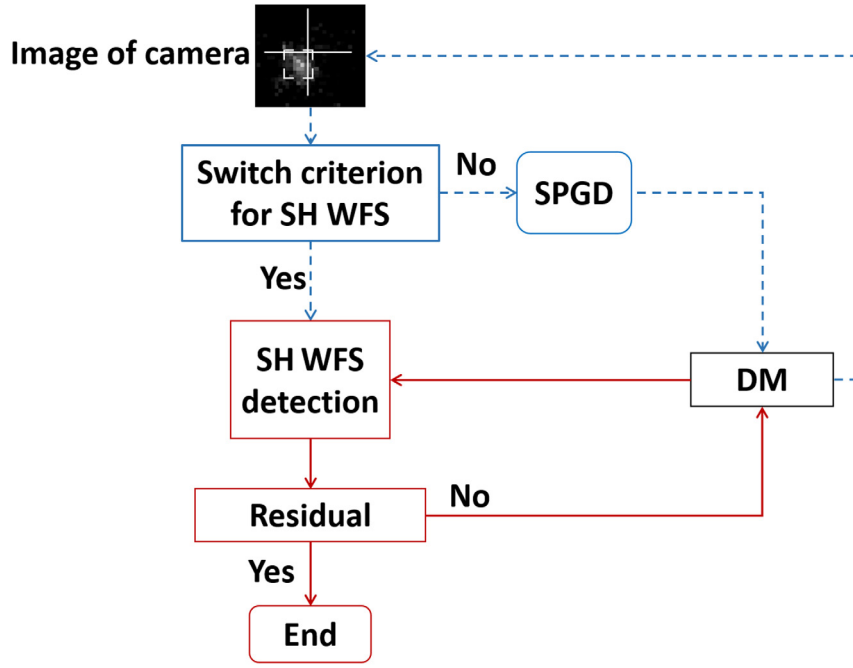


Fig. 2. Flow chart of the proposed method.

2.3. Switch criterion

From Fig. 2, we can see that the selection of the switch criterion is very important in ensuring the effectiveness of the proposed method. The switch criterion must effectively judge what time the SH WFS can measure the aberrations correctly. If the SH WFS can detect the aberrations, almost all the light spots imaged by the microlens array should be in the range of their corresponding area. Based on this condition, the image correlativity is chosen as the switch criterion: in the configuration of AOS, the light spot diagram of the SH WFS without the aberrations is used as a reference image, and the spot diagrams with aberrations are selected as the distorted images. The zero-mean cross correlation may be calculated with the reference and distorted images by using Equation [33]:

$$C_{ZMCC} = \frac{\sum_{i=1}^p \sum_{j=1}^q [f_0(x_{0i}, y_{0j}) - \bar{f}_0] [f'(x'_{i}, y'_{j}) - \bar{f}']}{\sqrt{\sum_{i=1}^p \sum_{j=1}^q [f_0(x_{0i}, y_{0j}) - \bar{f}_0]^2} \sqrt{\sum_{i=1}^p \sum_{j=1}^q [f'(x'_{i}, y'_{j}) - \bar{f}']^2}} \quad (7)$$

where the size of the reference and distorted images are $p \times q$ pixels; the gray level of the reference and distorted images are represented by $f_0(x_0, y_0)$ and $f'(x', y')$, respectively; and \bar{f} and \bar{f}' are the average gray levels of the reference and distorted images, respectively. This indicates that the larger the image correlativity, the greater the possibility for direct wavefront detection with SH WFS. To calculate the C_{ZMCC} , $4 \times p \times q$ times of subtraction, $3 \times p \times q$ times of multiplication, and $3 \times p \times q$ times of addition are needed. While a normal CPU is used to perform the calculation, the computation time is about $(10 \times p \times q)/10^9$ s. For the SH WFS with 90×90 pixels, which is used in this work, the computation time is about $81 \mu\text{s}$ which may be ignored.

To choose an effective value of C_{ZMCC} as the switch criterion, a simulation is performed first. The distorted wavefronts are produced with the Zernike form of the Kolmogorov turbulence model [34,35], and their mean value of root mean square (RMS) is about 6 rad. Assuming that the SH WFS has the microlens array of 12×12 , the concrete simulation and calculation process is shown in Fig. 3. First, the distorted wavefronts are produced with 36 Zernike modes, and the distorted image may be calculated using the Fourier transform

method. The distorted image (far left of 1st row, Fig. 3) is used as the input image of the SPGD algorithm, and the coefficients of the first 36 Zernike modes are used for the optimization. At each iteration step, the wavefront and image can be computed with the SPGD algorithm simultaneously. Then, the spot diagram of the SH WFS (third row of Fig. 3) may be calculated with the retrieved wavefront ϕ_{SPGD} , and the correlativity C_{ZMCC} between the reference and distorted spot diagram may be computed. Furthermore, the detected wavefront of SH WFS ϕ_{WFS} can also be computed according to the spot diagram shown in fourth row of Fig. 3. If the SH WFS can detect the wavefront correctly, the difference between ϕ_{SPGD} and ϕ_{WFS} should be very small, and its change tendency should be stable. Consequently, the residual $|\phi_{SPGD} - \phi_{WFS}|$ should be calculated at each iteration step to judge the switch point between the SPGD algorithm and SH WFS.

Fig. 4 shows the correlativity and residual as functions of the iterations at the correction process with the SPGD algorithm. As can be seen, the correlativity is enlarged with the increased iterations. However, the residual changes randomly when the iterations are less than 28. This illustrates that the SH WFS cannot detect the distorted wavefront normally while the iterations are less than 28 and the correlativity is smaller than 0.81. The residual is reduced stably if the iterations are more than 28, thus indicating that the SH WFS can detect the wavefront accurately, and the reduction of the residual is caused by the wavefront correction with the SPGD algorithm. Although only a single simulated result is given in Fig. 4, actually, over 20 trials have been conducted; moreover, the switch point is at the correlativity of 0.81, but the iterations are different. All the simulated results show that the correlativity should be larger than 0.81 to detect the wavefront correctly with the SH WFS; thus, the correlativity of 0.81 is selected as the switch criterion.

3. Experiment

3.1. Optical setup

To validate the proposed method, an AOS established for the FSOC is used, as shown in Fig. 5 (the detailed information has been described in Ref. [36]). The communication and beacon beams are received by a telescope and then corrected by a tip-tilt mirror (TTM) and a DM,

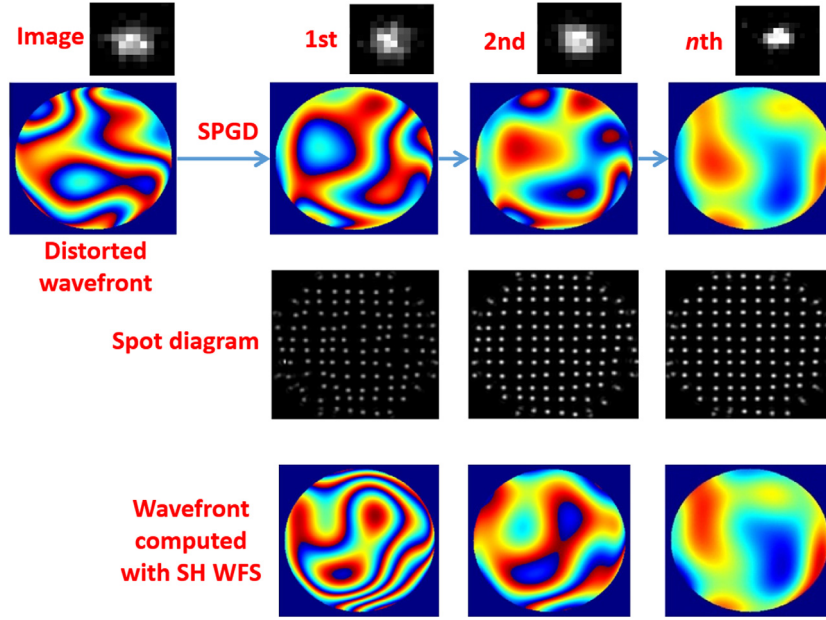


Fig. 3. Simulation of the correction process with the wavefront sensorless mode: the input image is produced with a distorted wavefront. The first row presents the images calculated with the retrieved wavefronts at the second row, and the third row presents the spot diagrams computed according to the retrieved wavefronts. The detected wavefront by SH WFS is calculated with the corresponding spot diagram.

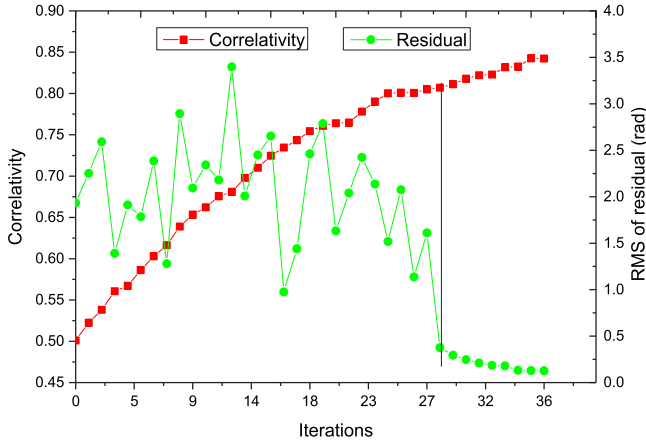


Fig. 4. Correlativity and residual as functions of iterations.

respectively. The camera is used to track the beacon light coming from the transmitting terminal. The SH WFS is used to measure the aberrations induced by the turbulence with the parameters of 15×15 microlenses and 1.5 kHz sampling frequency. The wavelengths of the signal and beacon light are 1550 and 808 nm, respectively. The coupling lens is used to couple the 1550 nm signal beam into the fiber. The 808 nm beacon light is split into two parts: one goes into the SH WFS for wavefront detection and the other is imaged by the tracking camera. To produce the strong turbulence, two atmospheric turbulence simulators are utilized with the atmospheric coherence lengths of 1 and 0.7 mm, respectively. In order to produce strong turbulence, two turbulence simulators are placed at the location of the yellow curves, as shown in Fig. 5. The optical power meter is used to measure the coupling efficiency of the fiber. In the paper, the BER is calculated by using the measured coupling efficiency [22,37]:

$$\langle BER \rangle = \frac{1}{2} \operatorname{erfc} \left(\sqrt{18 \times CE} \right), \quad (8)$$

here CE is the coupling efficiency, and $\operatorname{erfc}(x) = 1 - \frac{2}{\sqrt{\pi}} \int_0^x \exp(-z^2) dz$.

3.2. Static turbulence correction

While the turbulence simulator has not been moved into the optical layout, the system aberration is measured by the SH WFS, as shown in Fig. 6(a). The spot diagram is also saved as the reference image, as shown in Fig. 6(b). The image observed by the camera is shown in Fig. 6(c); this indicates that the system aberration may be ignored. Moreover, the coupling efficiencies of fiber and the BER are measured at 0.82 and 10^{-8} , respectively.

Before correction, two turbulence simulators are moved into the optical setup to produce strong turbulence. The spot diagram and measured wavefront of the SH WFS are shown in Fig. 7(a) and (b), respectively. As can be seen, the light spots in the surrounding areas with yellow dash lines present the abnormal forms: some exceed the corresponding sub-areas, while some occupy the entire corresponding sub-areas. Consequently, the centroid cannot be calculated correctly and the reconstructed wavefront (shown in Fig. 7(b)) is incorrect. Furthermore, the intensity of the image acquired by the camera is weak, and the light disk is confused. The calculated results show that the correlativity is 0.6, the coupling efficiency is 0.01, and the BER is 10^{-1} . First, to verify the effectiveness of the switch criterion, the closed loop correction is performed with the wavefront sensorless mode, and the first 7 Zernike modes are used to retrieve the wavefront. To achieve the distorted wavefront, the SPGD algorithm is operated according to Eqs. (4) and (5) by using the image shown in Fig. 7(c). According to the correction process shown in Fig. 3, the correlativity and wavefront RMS detected by the SH WFS as functions of iterations are acquired, as shown in Fig. 8. As can be seen, while the iterations are less than 46, the detected aberrations change randomly; however, the correlativity is increased accordingly while the iterations are raised. The results indicate that the SH WFS cannot detect the wavefront correctly. A jump phenomenon of the detected wavefront occurs at 46 iterations, and the correlativity is 0.81; after this point, the detected wavefront RMS is decreased and the correlativity is increased gradually. These results illustrate that the SH WFS can detect the aberration correctly if the correlativity is more than 0.81. Therefore, the correlativity switch criterion is valid with the value of 0.81.

By using the correlativity switch criterion value of 0.81, the correction of static turbulence is performed according to proposed method

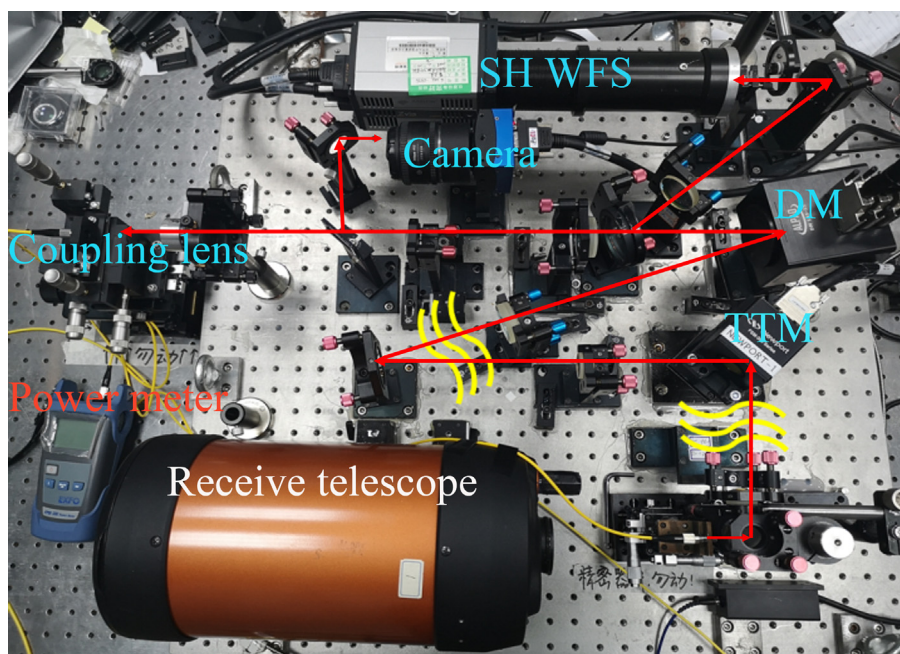


Fig. 5. Optical layout for AOS of the FSOC.

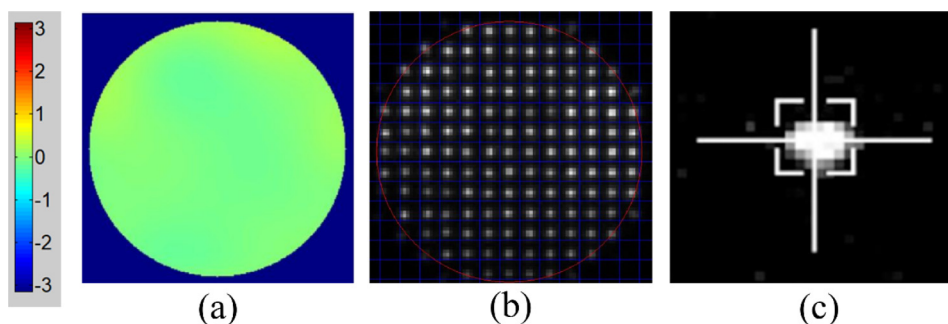


Fig. 6. AOS without the aberrations: (a) Wavefront; (b) Reference spot diagram; (c) Image.

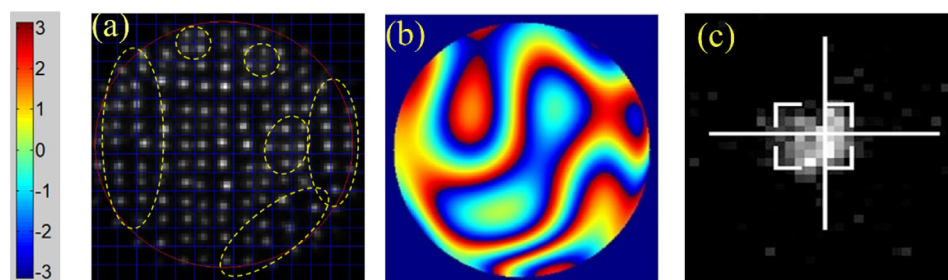


Fig. 7. AOS with static turbulence: (a) Spot diagram; (b) Measured wavefront by SH WFS; (c) Image.

shown in Fig. 2. The corrected results are shown in Fig. 9. When the correlativity is 0.81, the spot diagram (Fig. 9(a)) shows that almost all the light spots are within their sub-areas. As a result, the aberrations can be measured properly, as shown in Fig. 9(b). Compared with Fig. 7(c), the image intensity shown in Fig. 9(c) is increased as the aberration is reduced by adaptive correction with the wavefront sensorless mode. Then, the adaptive correction is switched to the SH WFS mode, and the aberrations are decreased further. After performing the adaptive correction, the correlativity of the spot diagram (Fig. 9(d)) is improved to 0.94, and the image intensity is increased apparently, as shown in Fig. 9(f). The RMS of aberrations is reduced to 0.75 rad,

but some aberrations still exist, as shown in Fig. 9(e). This is because the amplitude of the aberrations is too large, and some actuators have reached their maximum voltages. This means that a large dynamic range DM is needed for strong turbulence. Moreover, the coupling efficiency of the fiber is 0.55, and the BER is 3×10^{-6} .

3.3. Dynamic turbulence correction

The adaptive correction experiment of dynamic atmospheric turbulence is performed based on the proposed method, and the Greenwood frequency of 50 Hz is produced by rotating the turbulence screen. Using the correlativity switch criterion of 0.81, the adaptive correction

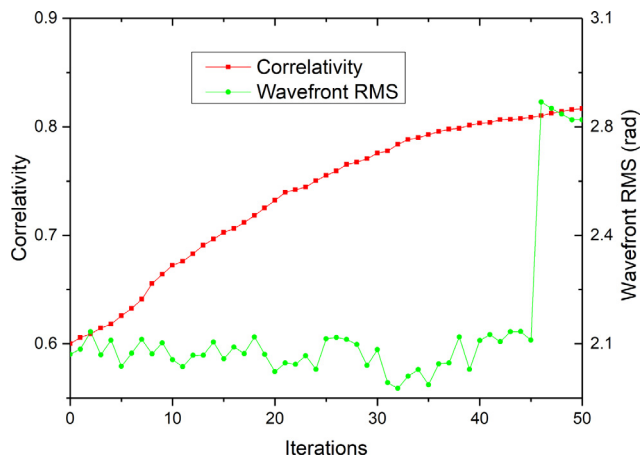


Fig. 8. Correlativity and RMS of the measured wavefront as functions of iterations.

is done by combining the wavefront sensorless and SH WFS modes. With the adaptive correction, the change of correlativity and detected wavefront RMS are presented in Fig. 10. Compared with Eqs. (4) and (8), the iterations is replaced with the correction time to visually illustrate the correction speed of the distortions. As Fig. 10(a) indicates, with the correlativity of more than 0.81, the correction changes to the SH WFS mode and the correlativity initially increase rapidly to 0.95 or so before eventually stabilizing at 0.95 with a little fluctuation. Initially, the detected RMS value of the aberration is random, because the SH WFS cannot measure the wavefront correctly. However, when the correlativity is larger than 0.81 and when the SH WFS can already accurately detect the wavefront, the RMS decreases drastically and then stabilizes at 0.75 rad with small deviation. These results illustrate that, for the dynamic turbulence, the proposed method can still switch the correction mode properly and correct the turbulence effectively.

The communication performance is also measured along with the adaptive correction. The coupling efficiency and communication BER as functions of correction time are shown in Fig. 11. As can be seen, the coupling efficiency is increased before stabilizing at 0.55 or so; furthermore, the BER is reduced continuously before stabilizing at

about 4×10^{-6} . Consequently, the proposed method may be used to improve the detection and correction abilities of the designed AOS for the FSOC, thereby lengthening the effective communication time.

4. Conclusions

The combination of the wavefront sensorless and SH WFS methods to avoid the amplitude of turbulence exceeding the designed range of SH WFS is proposed and demonstrated in this work. The realization scheme is presented, and the wavefront sensorless method is used to detect the turbulence distortions while the amplitude exceeds the detection range of SH WFS. The aberrations are corrected simultaneously by the DM according to the detected signal, which weakens the turbulence. A switch criterion, namely, the correlativity of 0.81 between the reference and distorted spot diagrams of SH WFS, is utilized to judge whether the SH WFS can detect the distortions correctly. While the aberration is detected by the SH WFS, the adaptive correction is performed with high frequency and accuracy. The SPGD algorithm is used to retrieve the wavefront, and the simulation results show that the detection mode can be switched effectively.

In order to validate the proposed method, an experiment is conducted in the laboratory to correct the simulated atmospheric turbulence. An AOS designed for FSOC is used simultaneously with a tracking camera to obtain the distorted images used to retrieve the wavefront. A static aberration is first detected and corrected with its magnitude exceeding the detection ability of SH WFS. The effectiveness of the switch criterion is verified, and the detection mode is switched while the correlativity increased to 0.81. Then, the correction is performed further with the SH WFS detection mode. After correction, the communication BER is reduced from 10^{-1} to 3×10^{-6} , and the correlativity of the spot diagram increased from 0.6 to 0.94.

In addition, the dynamic turbulence is also corrected with the proposed method with the Greenwood frequency of 50 Hz. The detection mode is still switched with the correlativity of 0.81. The results show that, while the SH WFS mode is used, the RMS value of the aberration decreased drastically before stabilizing at 0.75 rad or so. Furthermore, the communication BER is reduced continuously before stabilizing at about 4×10^{-6} .

All the results indicate that the proposed method may be used to solve the problem of the turbulence exceeding the designed range

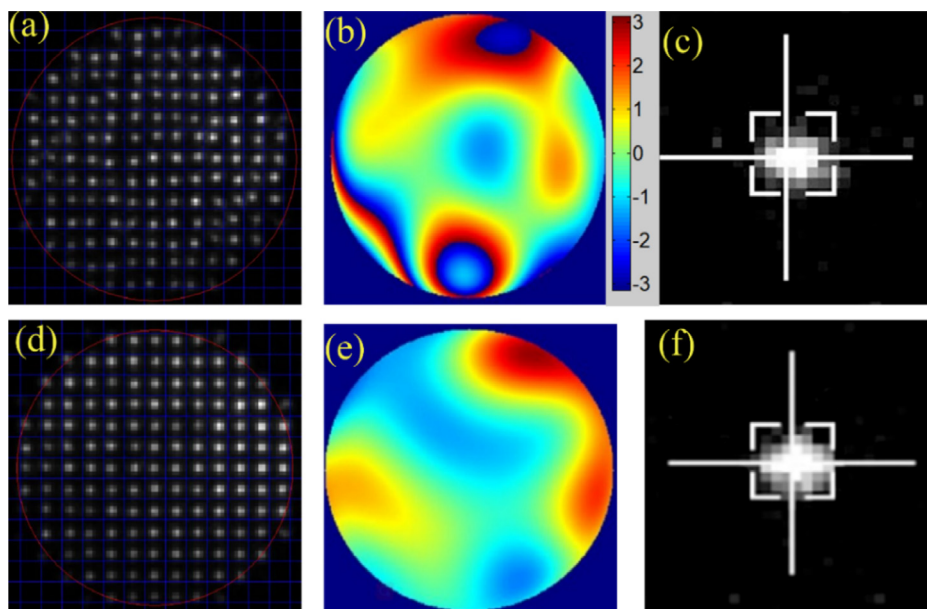


Fig. 9. Static turbulence with correction: the upper part presents the correction results for the SPGD method with the correlativity of 0.81 and the (a) Spot diagram, (b) Wavefront, and (c) Image. The lower part presents the correction results with SH WFS and the (e) Spot diagram, (f) Wavefront and (g) Image.

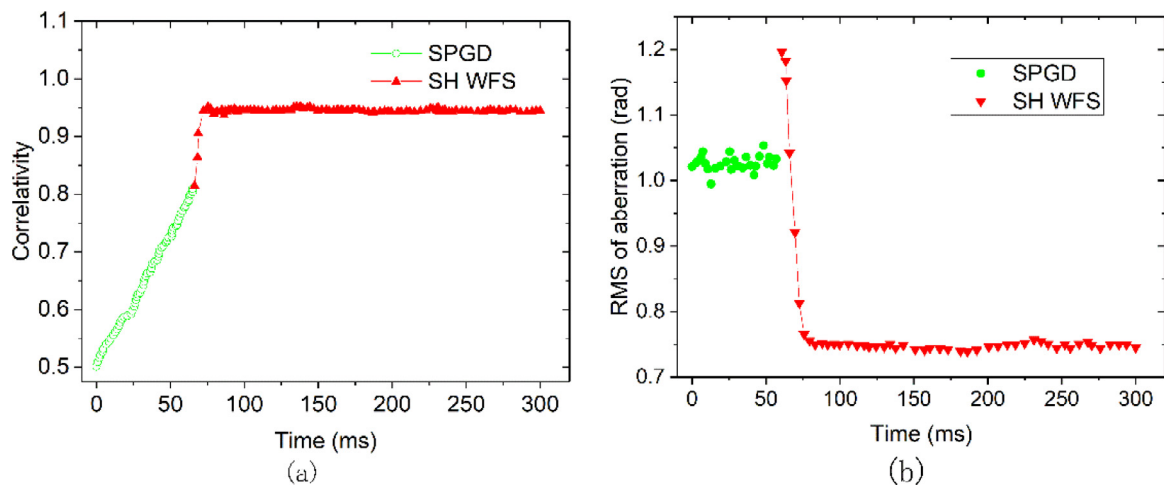


Fig. 10. Correction of dynamic turbulence: the correlativity (a) and RMS of corrected wavefront (b) as functions of the correction time.

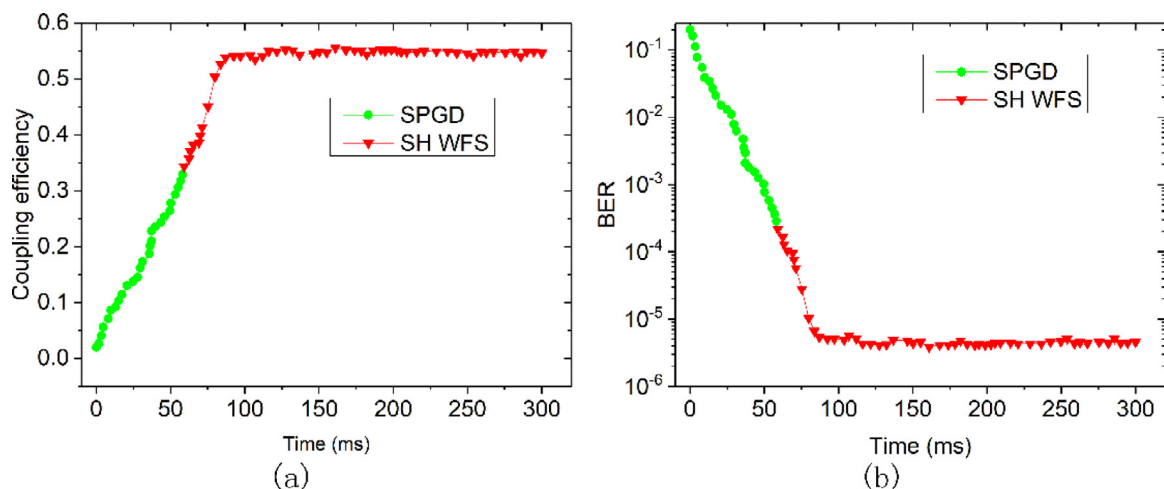


Fig. 11. Communication performance: the coupling efficiency (a) and BER (b) as functions of correction time.

while the AOS is used for the FSOC. Thus, the effective communication time is lengthened considerably, and the application fields are likewise extended. Therefore, this work is very helpful in implementing the AOS in FSOC applications.

Declaration of competing interest

The authors declare that they have no known competing financial interests or personal relationships that could have appeared to influence the work reported in this paper.

Acknowledgment

This work is supported by the Jiangsu Key Disciplines of the Thirteenth Five-Year Plan, China under Grant No. 20168765.

References

- [1] W.S. Rabinovich, C.I. Moore, R. Mahon, P.G. Goetz, H.R. Burris, M.S. Ferraro, J.L. Murphy, L.M. Thomas, G.C. Gilbreath, M. Vilcheck, Free-space optical communications research and demonstrations at the U.S. Naval Research Laboratory, *Appl. Opt.* 54 (31) (2015) F189–F200.
- [2] L.C. Andrews, R.L. Phillips, *Laser Beam Propagation through Random Media*, SPIE, 2005.
- [3] R. Lange, B. Smutny, B. Wandernoth, R. Czichy, D. Giggenbach, 142 km, 5.625 Gbps free-space optical link based on homodyne BPSK modulation, in: *Proc. SPIE* 2006, Vol. 6105, 61050A.
- [4] Abhijit Biswas, Juan M. Ceniceros, Matthew Jarrod Novak, Muthu Jeganathan, Angel Portillo, David M. Erickson, Jon De Pew, Babak Sani, James R. Lesh, 45-km horizontal-path optical link experiment, in: *Proc. SPIE*, Vol. 3615, 1999, pp. 43–53.
- [5] A. Belmonte, A. Rodríguez, F. Dios, A. Comerón, Phase compensation considerations on coherent free-space laser communications system, in: *Proc. SPIE* 2007, Vol. 6736, 67361A.
- [6] A. Belmonte, Influence of atmospheric phase compensation on optical heterodyne power measurements, *Opt. Express* 16 (9) (2008) 6756–6767.
- [7] J. Libich, J. Perez, S. Zvanovec, Z. Ghassemlooy, R. Nebuloni, C. Capsoni, Combined effect of turbulence and aerosol on free-space optical links, *Appl. Opt.* 56 (2) (2017) 336–341.
- [8] R.K. Tyson, D.E. Canning, Indirect measurement of a laser communications bit-error-rate reduction with low-order adaptive optics, *Appl. Opt.* 42 (21) (2003) 4239–4243.
- [9] R.K. Tyson, D.E. Canning, J.S. Tharp, Measurement of the bit-error rate of an adaptive optics, free-space laser communications system, part 1: tip-tilt configuration, diagnostics, and closed-loop results, *Opt. Eng.* 44 (44) (2005) 096003.
- [10] R.K. Tyson, J.S. Tharp, D.E. Canning, Measurement of the bit-error rate of an adaptive optics, free-space laser communications system, part 2: multichannel configuration, aberration characterization, and closed-loop results, *Opt. Eng.* 44 (44) (2005) 096003.
- [11] Yoshinori Arimoto, Morio Toyoshima, Masahiro Toyoda, Tetsuo Takahashi, Motokazu Shikatani, Kenichi Araki, Preliminary result on laser communication experiment using (ETS-VI), in: *Proc. SPIE*, Vol. 2381, 1995, pp. 151–158.
- [12] D.M. Boroson, A. Biswas, B.L. Edwards, MLC: Overview of NASA's Mars laser communications demonstration system, in: *Proc. SPIE*, Vol. 5338, 2004, pp. 16–28.

- [13] Thomas Berkefeld, Dirk Soltau, Reinhard Czichy, Edgar Fischer, Bernhard Wandernoth, Zoran Sodnik, Adaptive optics for satellite-to-ground laser communication at the 1m Telescope of the ESA Optical Ground Station, Tenerife, Spain, in: Proc. SPIE, Vol. 7736, 2010, pp. 146–153.
- [14] Jason B. Stewart, Daniel V. Murphy, John D. Moores, Andrew S. Fletcher, Keith M. Bonneau, Comparing adaptive optics approaches for NASA LCRD Ground Station #2, in: Proc. SPIE 2013, Vol. 8610, 86100M.
- [15] C. Petit, N. Vedrenne, V. Michau, G. Artaud, J.-L. Issler, E. Samain, M. Toyoshima, M. Akioka, D. Kolev, Y. Munemasa, H. Takenaka, N. Iwakiri, Adaptive optics results with SOTA, in: IEEE International Conference on Space Optical Systems and Applications, 2016, pp. 1–7.
- [16] A.K. Majumdar, J.C. Ricklin, *Free-Space Laser Communications: Principles and Advances*, Springer, 2008.
- [17] Juan C. Juarez, David W. Young, Joseph E. Sluz, James L. Riggins, David H. Hughes, Free-space optical channel propagation tests over a 147-km link, in: Proc. SPIE 2011, Vol. 8038, 80380B.
- [18] R.K. Tyson, Adaptive optics and ground-to-space laser communications, *Appl. Opt.* 35 (19) (1996) 3640–3646.
- [19] L. Zuo, A. Dang, Y. Ren, H. Guo, Performance of phase compensated coherent free space optical communications through non-Kolmogorov turbulence, *Opt. Commun.* 284 (2011) 1491–1495.
- [20] M. Li, M. Cvijetic, Coherent free space optics communications over the maritime atmosphere with use of adaptive optics for beam wavefront correction, *Appl. Opt.* 54 (2015) 1453–1462.
- [21] C. Liu, S. Chen, X. Li, H. Xian, Performance evaluation of adaptive optics for atmospheric coherent laser communications, *Opt. Express* 22 (2014) 15554–15563.
- [22] X. Yin, R. Wang, S. Wang, Y. Wang, C. Jin, Z. Cao, L. Xuan, Evaluation of the communication quality of free-space laser communication based on the power-in-the-bucket method, *Appl. Opt.* 57 (2018) 573–581.
- [23] B. Martin Levine, Elizabeth A. Martinsen, Allan Wirth, Andrew Jankevics, Manuel Toledo-Quinones, Frank Landers, Theresa L. Bruno, Horizontal line-of-sight turbulence over near-ground paths and implications for adaptive optics corrections in laser communications, *Appl. Opt.* 37 (1998) 4553–4560.
- [24] M.A. Vorontsov, G.W. Carhart, J.C. Ricklin, Adaptive phase-distortion correction based on parallel gradient-descent optimization, *Opt. Lett.* 22 (12) (1997) 907–909.
- [25] T. Weyrauch, M.A. Vorontsov, Free-space laser communications with adaptive optics: Atmospheric compensation experiments, *J. Opt. Fiber Commun. Rep.* 1 (4) (2004) 355–379.
- [26] W. Thomas, M.A. Vorontsov, Atmospheric compensation with a speckle beacon in strong scintillation conditions: directed energy and laser communication applications, *Appl. Opt.* 44 (30) (2005) 6388–6401.
- [27] J.R. Fienup, Phase retrieval algorithms: a comparison, *Appl. Opt.* 21 (1982) 2758–2769.
- [28] J.R. Fienup, Phase retrieval algorithms: a personal tour [Invited], *Appl. Opt.* 52 (2013) 45–56.
- [29] Piotr Piatrou, Michael Roggemann, Beaconless stochastic parallel gradient descent laser beam control: numerical experiments, *Appl. Opt.* 46 (27) (2007) 6831–6842.
- [30] M.A. Vorontsov, V.P. Sivokon, Stochastic parallel-gradient-descent technique for high-resolution wave-front phase-distortion correction, *J. Opt. Soc. Amer. A* 15 (10) (1998) 2745–2758.
- [31] Mikhail A. Vorontsov, Gary W. Carhart, Marc Cohen, Gert Cauwenberghs, Adaptive optics based on analog parallel stochastic optimization: analysis and experimental demonstration, *J. Opt. Soc. Amer. A* 17 (8) (2000) 1440–1453.
- [32] J.C. Spall, Multivariate stochastic optimization using a simultaneous perturbation gradient approximation, *IEEE Trans. Automat. Control* 37 (1992) 332–341.
- [33] B. Pan, Recent progress in digital image correlation, *Exp. Mech.* 51 (2011) 1223–1235.
- [34] R.J. Noll, Zernike polynomials and atmospheric turbulence, *J. Opt. Soc. Amer.* 66 (1976) 207–211.
- [35] N.A. Roddier, Atmospheric wavefront simulation using Zernike polynomials, *Opt. Eng.* 29 (1990) 1174–1181.
- [36] Rui Wang, Yukun Wang, Chengbin Jin, Xianghui Yin, Shaoxin Wang, Chengliang Yang, Zhaoliang Cao, Quanquan Mu, Shijie Gao, Li Xuan, Demonstration of horizontal free-space laser communication with the effect of the bandwidth of adaptive optics system, *Opt. Commun.* 431 (2019) 167–173.
- [37] R.G. Gallager, *Principles of Digital Communication*, Cambridge University, 2008.